Nanoscale

PAPER

View Article Online
View Journal | View Issue

Cite this: *Nanoscale*, 2016, **8**, 8737

The interaction with gold suppresses fiber-like conformations of the amyloid β (16–22) peptide†

Luca Bellucci,*[a,b] Albert Ardèvol,[c,d] Michele Parrinello,[c,d] Helmut Lutz,[e] Hao Lu,[e] Tobias Weidner[e] and Stefano Corni*[b,d]

Received 24th February 2016,
Accepted 14th March 2016

DOI: 10.1039/c6nr01539e

www.rsc.org/nanoscale

Inorganic surfaces and nanoparticles can accelerate or inhibit the fibrillation process of proteins and peptides, including the biomedically relevant amyloid β peptide. However, the microscopic mechanisms that determine such an effect are still poorly understood. By means of large-scale, state-of-the-art enhanced sampling molecular dynamics simulations, here we identify an interaction mechanism between the segments 16–22 of the amyloid β peptide, known to be fibrillogenic by itself, and the Au(111) surface in water that leads to the suppression of fiber-like conformations from the peptide conformational ensemble. Moreover, thanks to advanced simulation analysis techniques, we characterize the conformational selection *vs.* induced fit nature of the gold effect. Our results disclose an inhibition mechanism that is rooted in the details of the microscopic peptide–surface interaction rather than in general phenomena such as peptide sequestration from the solution.

1. Introduction

The heptapeptide $A\beta_{16-22}$ (sequence: KLVFFAE)‡ is a fragment from residue 16 to residue 22 of the full-length amyloid β peptide (Aβ).[1] The latter (featuring various alloforms, the most important being $A\beta_{40}$ and $A\beta_{42}$) is the basic constituent of the amyloid plaque characteristic of Alzheimer's disease.[2] In aqueous solution $A\beta_{16-22}$ does not have a specific conformation, but it is able to aggregate into amyloid fibrils with high β-sheet structure content.[3,4] Because of its propensity to self-assemble, $A\beta_{16-22}$ is well suited as a model system for probing the mechanisms of aggregation by using experimental[3–9] and theoretical[10–21] approaches. For example, it was possible to determine that $A\beta_{16-22}$ in aqueous solution self-assemble to form fibrils by a direct transition from a random coil state to a β-sheet structure.[9] The fibrillation process of $A\beta_{16-22}$ is promoted by the presence of the sequence LVFFA[22] which also constitutes the hydrophobic core of the full-length Aβ peptide. $A\beta_{16-22}$ represents therefore a key system to understand the more complex fibrillation processes of Aβ.

It is well-known that the fibrillation process of this (and of other) peptide can be affected by the environmental conditions. For example, the self-assembling of $A\beta_{16-22}$ can be manipulated by tuning the protonation state of the terminal residues (*i.e.*, K and E) by a pH change, and/or capping the charged terminal, that are hydrophilic groups.[5,12,23] At acidic pH the uncapped $A\beta_{16-22}$ peptides self-assembled into nanofibrils, whereas the capped ones formed nanotapes.[5] Recently, the interaction with nanoparticles (NPs) and inorganic surface[24,25] has been identified as a further environmental condition that can strongly affect the fibrillation propensity of peptides and proteins.[26] Depending on the nature of the nanoparticle and the protein/peptide considered, either acceleration or inhibition of the fibrillation process was obtained. Limiting ourselves to Aβ peptides, various NPs have been investigated, obtaining acceleration of fibrillation,[27–29] its retardation,[27,28,30–35] or both effects depending on the relative peptide/NP concentrations.[36,37] Despite the extensive experimental evidence, the underlying molecular mechanism determining the role of nanoparticle is mostly unknown. A general mechanism accelerating fibrillation has been proposed early:[38,39] when the nanoparticle binds the peptide/protein, the local concentration on the NP surface is higher than in solution, making the formation of critical fiber nuclei easier. In contrast, mechanisms leading to inhibition of folding are less general[36,37,40,41] and much less well-characterized. A con-

[a]*Dipartimento FIM, Università di Modena e Reggio Emilia, I-41125 Modena, Italy. E-mail: luca.bellucci_s3@unimore.it*
[b]*Centro S3, CNR-NANO Istituto Nanoscienze, I-41125 Modena, Italy. E-mail: stefano.corni@nano.cnr.it*
[c]*Department of Chemistry and Applied Biosciences, ETH-Zurich, Switzerland*
[d]*Facoltà di Informatica, Istituto di Scienze Computazionali, Università della Svizzera Italiana, CH-6900 Lugano, Switzerland*
[e]*Max Planck Institute for Polymer Research, D-55128 Mainz, Germany*

† Electronic supplementary information (ESI) available: Representative structures for the most populated conformational structures of $A\beta_{16-22}$ on bulk and on the metal surface. Normalized distribution of the variable *s* defined as the sum of internal dihedral angles of the peptide in solution and at the gold/water interface. See DOI: 10.1039/C6NR01539E

‡ K: lysine; L: leucine; F: phenylalanine; A: alanine; E: glutamic acid.

centration-dependent mechanism that has been suggested is the sequestration of the peptide from the solution.[37,42] Another important piece of information is that for peptides, the propensity to fibrillate is related to their propensity to assume fiber-like conformations at the single peptide level.[37,43,44] This has been established largely by coarse-grained simulations validated against experiments, also in the presence of surfaces.[37] Therefore, we propose that a mechanism leading to inhibition of fibrillation consists of the reduction of the population of fiber-like conformations upon interaction with the surface/nanoparticle.

We have recently demonstrated that the interaction with a gold surface can re-shape the internal free-energy landscape (and thus the conformational ensemble) of the prototypical alanine dipeptide.[45] To identify the effect of the interaction with inorganic materials on the conformational ensemble of a fibrillogenic peptide, we study the conformational ensemble of $A\beta_{16-22}$ in bulk solution and when adsorbed on the Au(111) surface by means of enhanced sampling atomistic simulations. Au(111) is the most stable surface of gold, and the most frequently occurring in nanoparticles.[46] In particular, we have used Parallel Tempering[47,48] combined with Metadynamics[49,50] to effectively explore the conformational space of the peptide, and its perturbation due to the interaction with gold. To characterize such multi-dimensional conformational space, we have analyzed the outcome of the simulations using a recently proposed dimensionality-reduction technique, called sketch-map analysis,[51–54] whose usefulness to interpret the behavior of complex polypeptides has been recently shown.[55] Fiber-like conformations turn out to be suppressed by the interaction with the surface, suggesting that inhibition of fibrillation is possible. Moreover, we could identify the molecular mechanism leading to this result. Our findings are corroborated by X-ray Photoelectron Spectroscopy (XPS) and Sum-Frequency Generation (SFG) experiments, and are in agreement with existing experimental evidence showing that inorganic species able to engage the LVFFA segment of Aβ, such as fullerenes,[56,57] are indeed able to inhibit fibrillation.

2. Methods and computational details

All simulations were performed with Gromacs[58] (v4.5.3) in conjunction with the PLUMED[59] (v1.3) plug-in. Analyses were performed with Gromacs tools and VMD.[60] The peptide and gold surface were treated with GolP FF,[61,62] a force field that was specifically parameterized to describe peptide–Au(111) surface interactions. GolP employs OPLS/AA for the peptide and that gave good results compared with experiments for the amyloid β peptide.[63,64] The initial conformation of the $A\beta_{16-22}$ segment (*i.e.* residues KLVFFAE) was extracted from the first NMR structure deposited at the protein data bank (PDB code 1IYT). The peptide was modeled in the zwitterionic form with an N-terminal of NH_3^+ and a C-terminal of COO^-; the lysine side-chain was protonated and the glutamic acid side chain was deprotonated.

The simulations were performed in explicit solvent using SPC[65] water. The total number of water molecules was 2773 in a rectangular box of dimensions $41 \times 41 \times 62$ Å^3. The simulations were conducted using periodic boundary conditions (PBC), in all the three dimensions. The long-range part of the electrostatic potential was treated with the Particle Mesh Ewald (PME) sum with a grid size of $42 \times 42 \times 64$. The cut off distance for non-bonded interactions was set to 10 Å and a switch function was applied to smooth interactions between 9 and 10 Å. The integration time step was set to 2 fs and all bonds were treated as holonomic constraints using the LINCS algorithm.[66]

The equilibration protocol consisted of several steps. First the peptide (*i.e.*, KLVFFAE) was placed in the middle of the box, which contains water and a gold slab (exposing the (111) face and composed of five layers) and was minimized by 3000 steps using the steepest descent algorithm. The coordinates thus obtained were used to perform 100 ps of MD simulation in the NVT ensemble (temperature 300 K) with protein heavy atoms restrained. 200 ps without restraints were then performed in the NPT ensemble (pressure 1 atm, temperature 300 K). The final conformation was used to perform 200 ps in the NVT (temperature 300 K) ensemble, obtained *via* the stochastic velocity-rescaling thermostat.[67]

2.1. Parallel-tempering metadynamics

Because of the large number of degrees of freedom and the different kinds of interactions of the system under study (*i.e.* protein–protein, protein–gold, protein–water *etc.*) the mere use of standard MD does not ensure a sufficient conformational sampling of the system (Fig. 1).

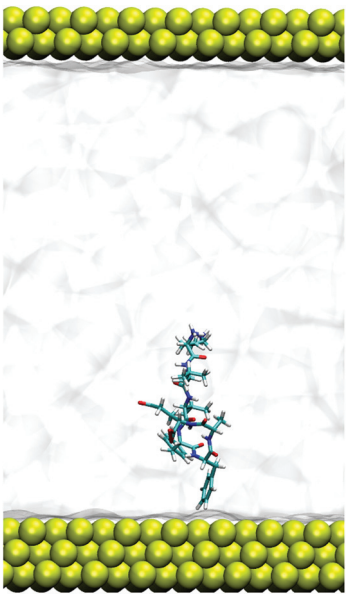

Fig. 1 Snapshot of the system during metadynamics simulation. The system is composed by water, $A\beta_{16-22}$ and five gold layers. Peptide can interact with two equivalent gold surfaces. CV is the *z* coordinate of the center of mass of the peptide with respect to the gold surfaces.

As already stated in the Introduction, to ensure an adequate sampling, we used Parallel Tempering[47,48] molecular dynamics together with MetaDynamics[49,50] (PTMTD). Following such a protocol, 16 copies of the system (replicas) are simulated concurrently at different temperatures (see below for details). Exchanges of the configurations of neighboring replicas are attempted at fixed intervals, and are accepted or rejected by means of a Metropolis test so as to ensure the correct sampling of the equilibrium ensemble. Using high temperatures it is possible to accelerate the crossing of the conformational energy barriers of the protein, and to have faster diffusion. In metadynamics, a history-dependent bias potential is added regularly during the simulation along some selected *collective variables* (CVs) so as to disfavor the visit of already visited states and enhancing the sampling. It is possible to demonstrate[50,68] that this bias converges to the free-energy landscape along the CVs, up to a constant.

To set up the enhanced sampling simulation, the last conformation obtained from the equilibration protocol was replicated 16 times. The replicas were simulated with parallel tempering (PT) for 2 ns; the temperatures of the replicas spanned between 300 and 366 K. The exchange between replicas was attempted every 300 steps, *i.e.* 0.6 ps.

Parallel-tempering metadynamics (PTMTD)[49] was performed starting from the replicas obtained by the previous parallel tempering equilibration. The setup of the parallel tempering protocol was the same as in the equilibration run. All replicas were simulated by metadynamics using as CV the projection along the z coordinate of the distance between center of mass (COM) of the peptide and the gold surface. In this way, surface and bulk-water conditions are sampled with statistically relevant probabilities. The width and the height of the Gaussian functions were set at 0.35 Å and 2 kJ mol^{-1} respectively. The bias potential was regularly updated at every 5 ps intervals throughout the simulation. After 78 ns of metadynamics the height of the Gaussian functions was scaled to 1 kJ mol^{-1} to refine the energy profile. Each replica was simulated for 140 ns yielding an aggregated total time of 2.2 μs. The mean acceptance ratio evaluated at the end of the PTMTD simulation was 18%. The reconstruction of the free-energy profiles was performed with the PLUMED plugin.[69] To estimate the accuracy of the reconstructed free energy profile, we first generated the free energy profiles (as the sum of the deposited hills) every 1 ns excluding the first 50 ns of metadynamics, then we aligned such profiles following the results of ref. 70 and finally, for selected COM–Au distances placed every 2 Å, we calculated the error by block-averaging the free-energies obtained for those distances at different times. The free energy of adsorption was obtained from the free-energy profile as described by Schneider *et al.*[71] Such a procedure requires to define the range of COM–Au distances corresponding to the adsorbed peptide. The lower boundary of this COM–Au distance range was here chosen to be 0; the higher boundary was chosen as the COM–Au distance where the free energy profile is 2.4 kJ mol^{-1} (*i.e.*, kT) below the bulk solution free-energy.

2.2. Setup of the sketch-map analysis

The analysis of the conformational ensemble of a flexible peptide as Aβ_{16-22} is far from being straightforward. Conformations are defined in a high dimensional space (even considering only the backbone dihedral angles Φ and Ψ, a 7 aa peptide like Aβ_{16-22} requires 12 angles, *i.e.*, a 12-dimensional space). While it is reasonable to suppose that the peptide conformations are still clustered in basins,[51] it is not obvious how to choose a manageably small set of order parameters (collective variables) that allows to discriminate them. Recently, a procedure to map the high-dimensional (high-D) conformational space to a 2D space by keeping the relevant elements of the high-D space structure has been proposed and successfully applied to problems in different fields.[51–54] The basic idea consists of: defining a distance between structures in the high-D space (here the circular distance in the backbone torsional angle space), associated to each conformation in the high-D space a point in the Cartesian (2D) space and arranging these points in such a way that the Euclidean distances between them reproduce at best (in a sense that will be clarified shortly) the distances in the high-D space.

In general it is not possible to preserve in the 2D space all the distances of the high-D space, so what is really required is that the high-D distances that are smaller than a typical, user-defined threshold length σ are mapped to 2D distances that are also smaller than σ, and *vice versa*. By judiciously choosing σ, and a few other numerical parameters that control the numerical mapping, the set of representative points distribute on the Cartesian plane conserving the main features of basins in the high-D space (for this property, such sets have been called *sketch-maps*), providing a manageable way to identify changes in the conformational ensemble as a response to external perturbations (such as the surface). We refer the reader to the original work[51] for a comparison of sketch-maps with other dimensionality reduction techniques such as principal component analysis.

Sketch-map analysis has been performed *via* the suite of programs distributed from the web-site http://epfl-cosmo.github.io/sketchmap/. A snapshot every 2 ps was saved from the trajectory of the lowest temperature replica in the PTMTD, and the values of the 12 backbone angles in each such snapshot was extracted. The high-D distance was defined as previously[51] and fully takes into account the dihedral angle periodicity. 1000 landmark points in the 12-dimensional space defined by these angles were selected according to the staged algorithm[54] with gamma = 0.1. Since the landmark points were selected from the whole trajectory (*i.e.* from the peptide-adsorbed, the peptide-solvated and the intermediate states), the same numerical transformation can be used to produce the sketch-maps associated to the conformational ensembles of all states, making their comparison straightforward. The sketch-map was built by minimizing the stress function reported in ref. 51 for the landmarks using a distance threshold σ = 2.5, and $a_D = b_D = 7$ for the sigmoid function of high-dimensional distances and $a_d = 2$, $b_d = 7$ for the sigmoid

function of bidimensional distances (see ref. 51 for definitions). σ, the most important parameter in defining the sketch-map, was determined by trial-and-error, $a_{D/d}$ and $b_{D/d}$ were chosen on the basis of previous experience and were not optimized further. The sketch-map that refers to bulk behavior was obtained from the projection on the 2D space of the PTMTD snapshots where the COM–gold distance was larger than 22 Å and the sketch-map for the peptide on the surface was obtained from snapshots where the COM–gold distance was ±1 Å of the minimum free-energy distance (4.7 Å).

2.3. XPS and SFG experiments

2.3.1. Sample preparation. $A\beta_{16-22}$ (2 mg) was dissolved in DMSO (33 μl) due to high aggregation tendencies in water or buffer. From this solution, the required volume for a final concentration of 1 mg ml^{-1} $A\beta_{16-22}$ was added to a vial with 1 ml of water on a gold coated silicon wafer (1.2 nm Cr and 50 nm Au). The gold substrate was incubated for 24 h in the peptide solution. To avoid Langmuir–Schäfer deposition of a film from surface adsorbed peptides when removing the sample, the solution was flushed out of the vial for 1 min with running MilliQ water. The gold substrate with the adsorbed peptide was taken out of the vial and rinsed for another 60 s with MilliQ water, then dried overnight. Self-assembled monolayers on gold for the normalization of SFG spectra were prepared in a similar way. A solution of dodecanethiol (DDT) was prepared in ethanol (5 mM). The solution was added to a gold coated silicon wafer in a glass vial and incubated overnight at room temperature. The next day the substrates were taken out of the solution and rinsed for 60 s with ethanol and then dried. The gold samples were stored under nitrogen until the measurement.

2.3.2. X-ray photoelectron spectroscopy. A Kratos AXIS Ultra DLD spectrometer with a monochromatic Al Kα X-ray source was used to collect the XPS data from the gold substrates. The electron take off angle was 90° (normal to surface). The acquisition was performed with an analyzer pass energy of 80 eV. The base pressure during the measurements was 5×10^{-9} mbar. The data was analyzed with the CasaXPS software.

2.3.3. Sum frequency generation. The SFG setup used to acquire spectra from the gold adsorbed peptides is described elsewhere.[72] In brief, a 10 W Spitfire Ace system (Spectra-Physics, SP) with a repetition rate of 1 kHz is pumped with two Empower systems (SP) and seeded with a Mai Tai (SP). A part of the beam is used to generate broad-band infrared light in a TOPAS Prime/NDFG unit (SP). The other part is spectrally narrowed to 800 nm with a bandwidth of ~16 cm^{-1} using an etalon. The infrared (IR) and 800 nm (VIS) pulses are overlapped spatially and temporally on the gold substrate with angles of incidence of 60° (IR) and 55° (VIS) to generate SFG in a reflection geometry. The acquired spectra were energy corrected using water vapor absorption bands and normalized using gold substrates with self-assembled monolayers of dodecanethiol. A linear background was subtracted. The SFG spectra calculation were performed using the formalism described by Roeters *et al.*[73]

3. Results and discussion

3.1. Adsorption free-energy profile

Adsorption free-energy profiles were calculated previously for other peptides[71] but not in the context of amyloidogenesis. The adsorption free energy profile along the chosen CV (the metal–peptide distance) is shown in Fig. 2. The profile has been obtained by averaging the results at the two gold/water interfaces present in the simulated system, the error bars represent the accuracy of the free energy calculated as described in the previous section.

In the range 1.5–2.5 nm, the interactions between the surface and the peptide are negligible. At 2.5 nm the peptide is equidistant from both gold surfaces and the corresponding free energy value was taken as zero. At 1.5 nm the peptide starts to interact with the metal surface and the free energy decreases. At lower distances the free energy profile shows some irregularities, different for the two interfaces. These irregularities might suggest that the peptide during the adsorption process can approach and finally adsorbs onto the gold surface in a series of different conformations/orientations. However, these irregularities are comparable to the extent of the error bars of the free energy, therefore no definitive conclusion can be drawn.

The absolute minimum is located at 0.47 nm from the gold surface. At this distance $A\beta_{16-22}$ is completely adsorbed onto the gold surface. We have calculated the adsorption free energy as discussed in ref. 71, obtaining a value of −62 ± 16 kJ mol^{-1}. There are no experimental data to compare directly with. Typical adsorption free-energy values for other dodecapeptides at polycrystalline (*vs.* single plane (111)) surfaces are in the same range but somewhat smaller, around −40 kJ mol^{-1}.[74,75] Certainly the presence of other Au faces in the experiments decreases the affinity with respect to Au(111),[76–78] and the highly charged nature of the experi-

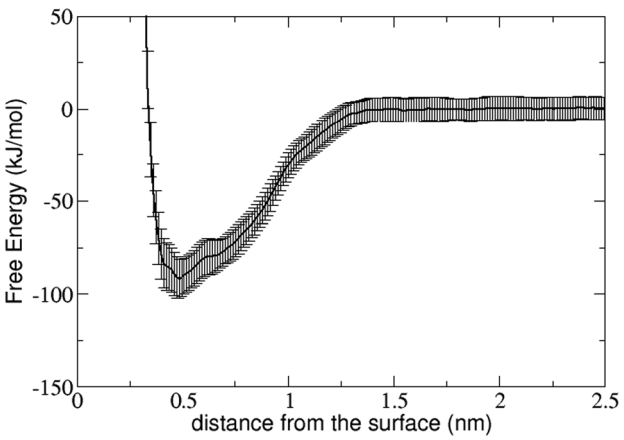

Fig. 2 Free energy adsorption profile of $A\beta_{16-22}$ onto the gold surface.

mentally measured dodecapeptides may also contribute to reduce their adsorption by creating unfavorable peptide–peptide Coulomb repulsion effects as well as substantially improving the solvation free energy. Finally, part of the difference may be due to the force field, since the original GolP force field tends to overestimate the binding free energies in solution with respect to the more recent GolP-CHARMM.[76,79]

3.2. Conformational analysis on the basis of the end-to-end distance

In this section we shall present an analysis of the conformational changes upon adsorption based on a standard collective variable for a floppy peptide, *i.e.*, the end-to-end distance. Although its descriptive power is quite limited, it provides a first glimpse of what happens to the peptide conformational ensemble. In the next section, we shall use instead an analysis technique specifically designed to study conformational ensembles and their changes. The end-to-end distance d of the peptide is here defined as the distance between the terminal C_α atoms (dotted red line in Fig. 3d).

The distribution of the end-to-end distance by the bias of the metadynamics as a function of the COM–gold distance is reported in Fig. 3. Not surprisingly, the end-to-end distance is not effective in defining the conformational basins in bulk solution: when the peptide is far from the surface, the distribution of end-to-end distance spans a large interval with a quite homogeneous distribution, possibly with a maximum around 0.8 nm and with a distinct region below 0.6 nm. Nevertheless, when the peptide comes closer to the surface, the distribution of end-to-end distance becomes more structured. We can recognize roughly 4 regions of end-to-end distances: (a) completely elongated with d greater than 1.2 nm, (b) partially elongated with d between 1 nm and 1.2 nm, (c) partially closed with d between 0.6 nm and 1 nm (Fig. 3(c) and (d)) completely closed (*i.e.* U shape)[80] with d lower than 0.6 nm (Fig. 3(d)). Visual inspection shows that within each d interval, various backbone conformations co-exist. It is worth noting that the partially closed conformations (Fig. 3(c)) are stabilized by a salt bridge between the long side chain of the LYS residues and the carboxylic groups of the C-terminal tail or GLU residue, whereas the completely closed conformations (Fig. 3(d)) are stabilized by a salt bridge between the N-terminal and the same carboxylic groups (*i.e.* C-terminal tail or GLU residue).

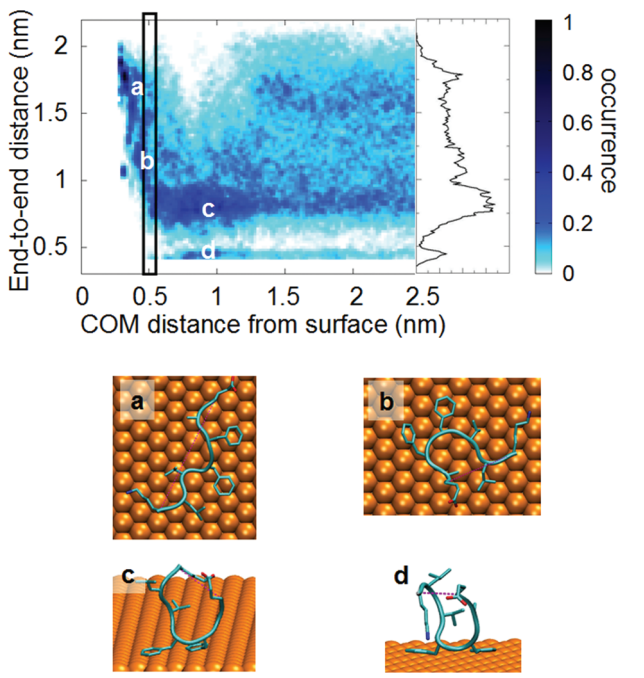

Fig. 3 Distribution fraction of the end-to-end distance d as a function of the peptide–gold distance (top). The black rectangle identifies the minimum of the free energy with respect to the peptide–surface distance. In the top right inset we show the distribution averaged over the bulk region (COM distance from the surface larger than 1.25 nm). Panels (a)–(d) show examples of conformations with characteristic d values. The end-to-end distance (d) is defined as the distance between the terminal C_α atoms. All the distances are in nm.

At short distances from the surface (closer than 1.2 nm) $A\beta_{16-22}$ starts to interact with the surface. Usually the FF motif (which shows high affinity towards the metal surface) is adsorbed to the surface, whereas charged groups (*i.e.* terminal residues) point towards the solvent. In this region the most populated states are the partially closed (Fig. 3(c)) and the closed conformers (Fig. 3(d)). The elongated conformers are not present.

At a distance lower than 0.5–0.6 nm the peptide is completely adsorbed and starts to populate the elongated and partially elongated conformer states (Fig. 3(c and d)). While end-to-end distance may convey some useful information, the picture of the peptide conformational ensemble that it provides is rather partial, and more advanced analysis techniques, like that presented in the next section, are needed.

3.3. Effect of the adsorption on the peptide conformations: conformational selection *vs.* induced fit

In the previous section, we have described some of the changes in the structural properties of the peptide as a function of the distance from the surface *via* the end-to-end distance. It is clear, from that analysis, that the conformational ensemble is modified upon adsorption on the surface. However, the use of a single, structural descriptor is certainly not enough to characterize the peptide conformations. Indeed, sketch-maps[51,54] will be used here to analyze the effect of the adsorption on the peptide conformations. Analogously to intrinsically disordered proteins and peptides that bind to a biological partner,[81,82] two extreme cases can be defined.[83] In *conformational selection*,[84] the "biological partner" (the surface here) would bind only a subset of the conformations that exist in solution; in *induced fit*,[85] it would instead induce new conformations that do not belong to conformational basins of bulk solution. The first issue that we shall address here is whether the interaction with the surface is akin to conformational selection, induced fit or an intermediate case.

The sketch-map for the molecule in solution (*i.e.*, when the COM–gold distance is greater than 2.1 nm) is presented in Fig. 4(a) in terms of normalized density of conformations. The conformations that characterize each basin are shown in Fig. S1,† showing that indeed the sketch-map preserves the basin repartition of the high-D space. Populations for the major basins are also given in Fig. S1;† none of the basins collect more than 10% of the total population, showing that this peptide is floppy and lacks a dominant conformation. Fig. 4(b) shows the sketch-map for the peptide on the surface (*i.e.*, when the COM is within ±1 Å from the COM–surface distance corresponding to the minimum of the free energy). First, by comparing the two sketch-maps in Fig. 4(a) and (b), we note that indeed the surface changes sizably the conformational ensemble of the peptide. The comparison between the two sketch-maps (in solution and on the surface) allows us to address the question whether the binding to the surface is more similar to conformational selection or to induced fit. First, we note that there are indeed peptide conformations in water that are conserved also on the surface, *i.e.*, some portion of the maps of Fig. 4(a) and (b) are similarly populated. In particular, the basin identified by the basin labeled 2 is the most populated both in solution and on the gold surface (with a similar population, around 10%), albeit the center of the basin undergoes a small shift in the CV plane. However, many other well populated basins in solution disappear on the gold surface (*e.g.*, basin 1), *i.e.*, many conformations that exist in solution are not bound by the surface. In this respect, the binding process resembles the conformational selection mechanism, where some conformations do not participate in the binding. On the other hand, a pure conformational selection would require the sketch-map at the surface to be a subset of that in water. This is clearly not the case since new spots (*i.e.*, conformational basins) appear on the surface sketch-map that are not present in bulk water (see, *e.g.*, the spot marked by arrow 3). Therefore, the surface is inducing new conformations, *i.e.*, an induce-fit mechanism is also at work. We can characterize the conformational ensemble changes due to the surface as intermediate between an induced fit and a conformational selection one.

To quantify the changes of the conformational ensemble continuously from bulk solution to the surface, we have calculated the Hellinger's distance between the sketch-map in bulk solution and those at various COM heights. The Hellinger distance $H[f,g]$ is a measure of the overlap of two normalized distributions $f(Q)$ and $g(Q)$, function of a set of variables Q:

$$H[f,g] = 1 - \int \mathrm{d}Q \sqrt{f(Q)g(Q)} \qquad (1)$$

It is symmetric with respect to f and g, and yields a number between 0 (identical distributions) and 1 (no overlap). All the structures of the peptide found at varying values of COM distance to the gold surface were projected on the sketch-map to obtain the conformational population density of all the possible intermediate ensembles. By applying this distance definition we were able to show that the sketch-map changes almost monotonically from solution to surface, as shown in Fig. 5.

The distance between two sketch-maps both taken in bulk solution but at different COM positions turns out to be 0.1 (rightmost values in Fig. 5). We can take this value as a measure of the statistical uncertainty on the sketch-maps (in fact, without statistical noise the distance between two sketch-maps both in bulk solution would be 0). This confirms that the changes in the sketch-map upon adsorption (reaching a Hellinger distance of 0.9, leftmost value of Fig. 5) are well-beyond the level of statistical noise.

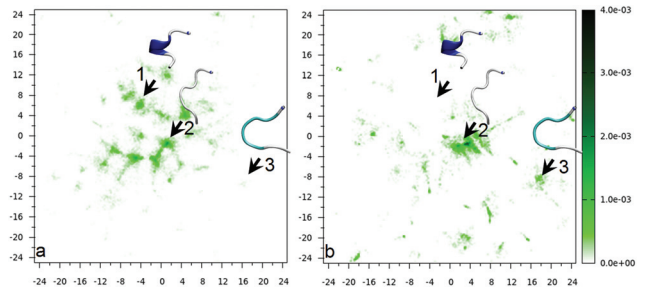

Fig. 4 Sketch-map for $A\beta_{16-22}$ in (a) bulk solution and (b) on the surface. The three arrows, labeled 1, 2 and 3, mark basins that change in three different ways passing from bulk to surface (1 is suppressed, 2 is almost unaffected – slightly shifted – and 3 is enhanced). Structures selected from the conformational basins 1, 2 and 3 are shown as insets in the panels. Representative structures for the other basins and basin populations are shown in Fig. S1.† The colour bar denotes the relative population.

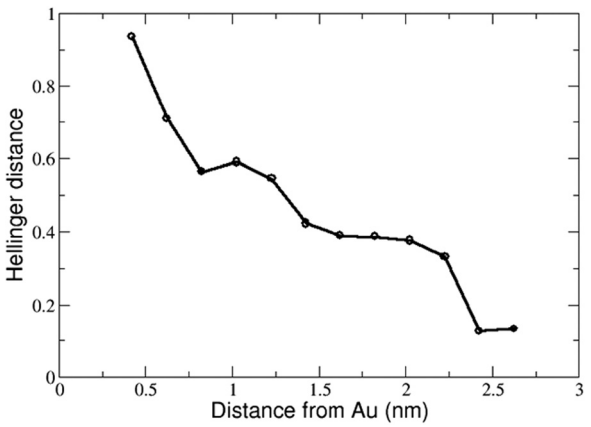

Fig. 5 The Hellinger distance between the sketch-map calculated at a given peptide COM–gold separation and the average sketch-map obtained in bulk solution. For each explored COM–gold separation, all the snapshots whose COM is within ±0.1 nm from that separation are considered to build the sketch-map. The Hellinger distance for the two rightmost points, that are in bulk solution and should be identical in the limit of infinite sampling, is around 0.1 and it is representative of the statistical uncertainty on sketch-maps obtained with the present level of sampling.

3.4. Effect of the adsorption on fibril-like conformations

The second issue that we want to address is whether the conformational space as modified by the surface is enriched or depleted of conformations that resemble amyloid fibers. To this end, we have calculated the backbone dihedral similarity s between an experimental structure of the peptide in a fiber and each member of the conformational ensembles of $A\beta_{16-22}$ in the bulk and on the surface. Such similarity s is defined as:

$$s = \frac{1}{2}\sum_i [1 + \cos(\phi_i - \phi_i^{\exp})] \quad (2)$$

where the sum runs on all the Ramachandran backbone angles considered, ϕ_i is the value of the i – angle in the PTMD conformation and $\phi_i^{\exp}$ is the same angle in the experimental structure. Here, the $\phi_i^{\exp}$ are taken by the experimental X-ray structures of $A\beta_{16-21}$ in fibers identified by the PDB ID 2Y29.[86] Other experimental structures (2Y2A, 3OW9,[86] and 3OVJ[87]) have very similar backbone angles. In the sum in eqn (2) we have considered all the Ramachandran dihedrals ϕ and ψ of the portion $A\beta_{16-21}$, ten angles in total. Therefore, s is equal to 10 when the PTMD snapshot is matching exactly the experimental backbone structure, and is decreasing toward 0 by decreasing the similarity between the PTMD snapshot and the experimental structure. The distributions of s for the bulk and the adsorbed conformational ensembles obtained by the PTMD simulations are shown in Fig. 6.

The most interesting region of such a plot is for s close to 10, *i.e.*, for perfect similarity with the experimental structure. First, it is apparent that in solution the peptide does assume fiber-like conformations (represented by the peak centred at $s \approx 9.5$), in agreement with its propensity to fibrillate. But the most important result comes from the on-surface distribution: the bulk peak at 9.5 fully disappears, showing that the adsorbed state is in fact strongly depleted of fiber-like conformations with respect to the water case. In other words, the interaction with the surface is suppressing fiber-like structures. It is also apparent that such population is replaced by new peaks in the region between 6.5 and 7.5 (*i.e.*, having several backbone angles far from those in the fibers).

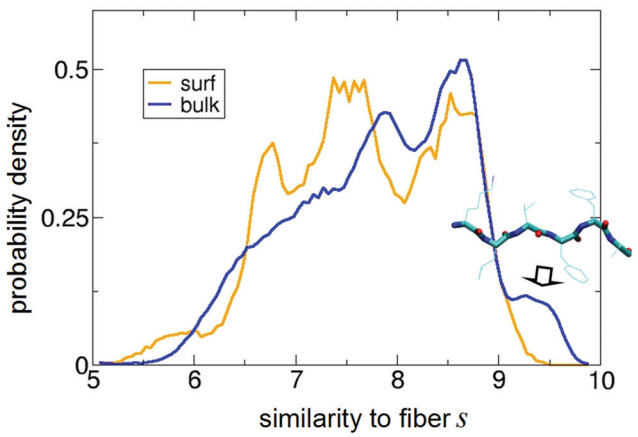

Fig. 6 Normalized distribution of s obtained for the peptide on the surface ("surf") and in bulk water ("bulk"). s = 10 corresponds to perfect matching with the backbone angles of the 2Y29 fiber structure of $A\beta_{16-21}$.[86] In the inset, a representative PTMD structure with s = 9.6 is shown. It highlights the clear β-strand (*i.e.*, fiber-like) character of the conformations contributing to the peak indicated with the arrow.

To strengthen our analysis, we have also projected all the existing experimental fiber structures on the sketch-maps in the bulk and on the surface. The results, reported in Fig. S2,† show that fiber-like structures sit in sketch-map regions that are populated for the peptide in the bulk and empty for the adsorbed peptides, confirming the picture just described.

This finding suggests that the intrinsic effect of the surface is to inhibit fiber formation, although one should not forget a possible opposite effect due to the increased local concentration of peptides following the adsorption from the solution of several peptide molecules.[39] The free-energy profile in Fig. 2, in fact, shows that the surface has a high propensity to bind $A\beta_{16-22}$ from the solution.

What is the driving force of this fiber-conformation suppression? The affinity of Au(111) for PHE[88] and the presence of two contiguous PHE's in the $A\beta_{16-22}$ peptide suggest a role for such residues. We can define their relative orientation in terms of the angle α between the C_α–C_β bonds, as presented in Fig. 7(a). $\cos(\alpha) > 0$ means that the phenyl rings are on the same side of the molecule (parallel orientation) while $\cos(\alpha) < 0$ means they are on the opposite side (called also antiparallel orientation in the following). Experimental fiber structures have $\cos(\alpha)$ close to −1 (Fig. 7(b)). By coloring the projections on the sketch-map of the PTMTD snapshots by the value of such $\cos(\alpha)$ (Fig. 7(d)), it turns out that the conformations with different relative PHE orientations are well separated in the peptide conformational space (*i.e.*, sketch-map spots are homogeneously colored).

Interestingly, the comparison of the sketch-map in bulk (Fig. 7(d)) with the sketch-map on the surface (Fig. 7(e)) shows that α is indeed a good coordinate to identify conformations that are suppressed by the surface: most of the structures with antiparallel phenyl rings disappear on the surface, in favor of new parallel ones. The driving force is clear: the favorable simultaneous interaction of both phenyl rings with the surface is possible only when they are on the same side of the molecule; therefore, antiparallel structures, where this interaction is impossible, are comparatively disfavored. Moreover, the other residues in the peptide do not interact strongly with the gold surface, leading to the U-shaped conformation previously discussed (an example is shown in Fig. 7(c)).

To explore the conformational ensemble as described by the variable α, in Fig. 8(a) we present the 2D free energy surface as a function of the peptide distance from the surface and of $\cos(\alpha)$. The change in the free-energy topology passing from the bulk (right-hand portion of the color map) to the surface (left-hand part) is visible. To make it more clear, we report in Fig. 8(b) the distribution of $\cos(\alpha)$ averaged for the two regions identified as "bulk" and "surf" in panel (a). It is evident that the interaction with the surface does change the relative population of parallel and antiparallel phenyl orien-

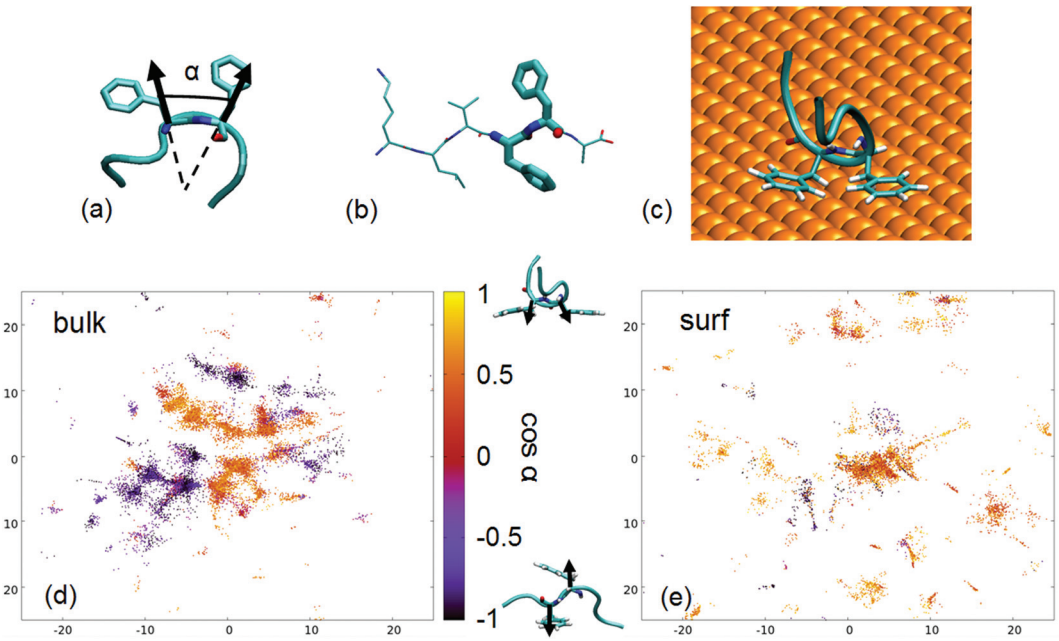

Fig. 7 (a) Definition of the angle α used to describe the relative orientation of PHE side chains; (b) representation of a fiber-like conformation of the peptide $A\beta_{16-21}$, from PDB 3OVJ[87] with PHE residues in thicker licorice representation; (c) an example of antiparallel, U-shaped conformation taken from the PTMTD; (d) sketch-map projections of the PTMTD trajectory snapshots where $A\beta_{16-22}$ is in bulk water on the sketch-map CVs, colored as cos(α); (e) sketch-map projections of the PTMTD trajectory snapshots where $A\beta_{16-22}$ is on the gold surface, colored as cos(α).

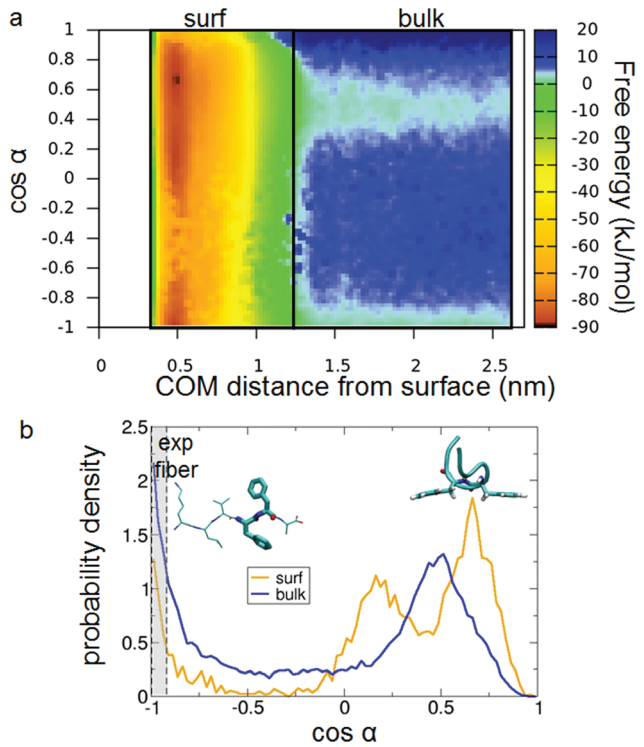

Fig. 8 (a) Color map showing the free energy surface for $A\beta_{16-22}$ as a function of the peptide COM distance from gold of the cosine of the angle α that identifies the relative orientation of the two PHE's. (b) Normalized distributions of cos(α) obtained for the peptide on the surface (region "surf" in panel (a)) and in bulk water (region "bulk" in panel (a)). The shadowed region corresponds to the α angles found in experimental fiber-structures.

tations, by suppressing the antiparallel (cos(α) < 0) conformations.

The range of variability of α in the experimental X-ray structures is identified as the gray region in Fig. 8(b). It is apparent also from this plot that in the on-surface distribution (blue curve in Fig. 8(b)) the region where experimental fibers sit is strongly depleted of conformations with respect to the bulk water case.

Interestingly, a permutation of the $A\beta_{16-22}$ residues leading to a sequence where the two PHE's are separated by an odd number of residue (*e.g.*, KLVFAFE) does not benefit by the potential inhibition mechanism described here, as the two PHE would be on the same side of a fiber-like conformation.

3.4.1. Comparison with experimental SFG data. To validate the computational predictions we have used XPS and SFG spectroscopy. First, XPS was used to determine the amount of $A\beta_{16-22}$ peptides adsorbed onto the gold surfaces. Table S1† summarizes the XPS-determined elemental composition of the $A\beta_{16-22}$ peptide film on gold adsorbed from a 1 mg ml^{-1} solution. Compared with published XPS spectra of surface protein films, the nitrogen concentration of 4.8 atom% indicates the formation of a monolayer film on the surface.[89] The composition of the peptide film omitting the gold emission is close to the theoretically expected composition of $A\beta_{16-22}$ peptides. The somewhat increased carbon content is likely explained by small amounts of residual advantageous carbon, which was not removed by the protein when binding. A very similar behavior is observed for monolayers of extended oligodentate molecules on gold.[90]

SFG was used to probe the conformation of $A\beta_{16-22}$ peptides on gold. The selection rules of SFG dictate that only ordered species at interfaces are visible in the SFG vibrational spectra.[91] SFG has been recently been developed into a reliable probe of interfacial folding and binding of peptides[92–94] and proteins.[95,96] For the experiments we adsorbed $A\beta_{16-22}$ peptides onto gold surfaces and recorded the spectra in the amide I region, which reports back on the secondary structure of protein backbones. The SFG spectrum shown in Fig. 9a exhibits a broad feature between 1620 and 1690 cm^{-1}, which is typical for the extended chain and strand motifs also observed in the simulations.[97] The presence of an SFG signal shows that the peptide film is reasonably well ordered and defined.[98]

For a more direct comparison of the simulations with the experimental data we calculated a theoretical SFG spectrum from a representative conformation for $A\beta_{16-22}$ at the surface (see Fig. 9b). This conformation is taken at the center of the most densely populated region of the on-surface sketch-map, Fig. 4(b). For the spectra calculations we followed a procedure described by Roeters *et al.*[73] The calculated spectrum, shown in the top panel of Fig. 9a, captures the broad shape and the energy position of the experimental peak very well, which shows a remarkable agreement of the SFG experiment and the MD simulations. The SFG spectra obtained from structures representative of bulk-like conformations did not provide such agreement (see Fig. S3†).

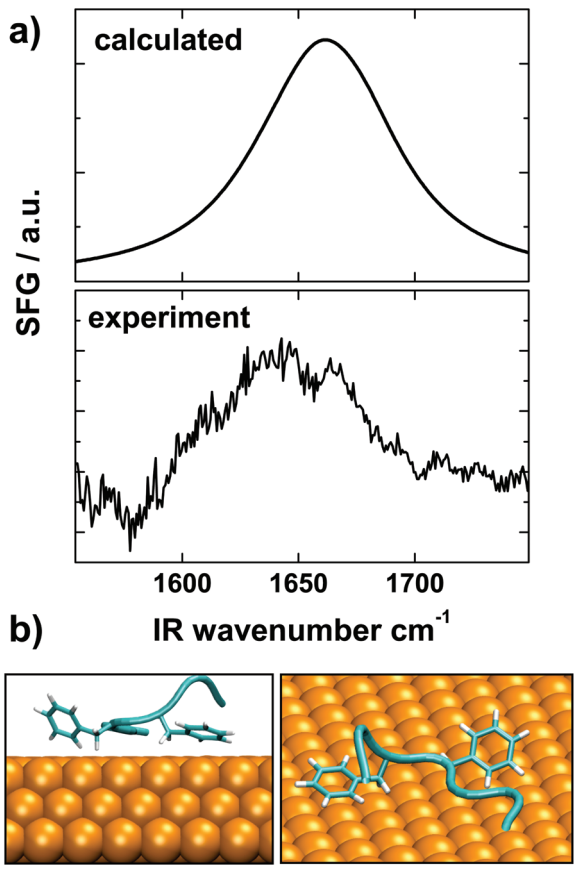

Fig. 9 (a) Comparison of experimental SFG spectra of $A\beta_{16-22}$ adsorbed onto gold surfaces and a spectrum calculated from the structure shown in panel (b). The calculated spectrum agrees well with the experimental data. (b) Snapshot of the simulated structure used for the spectra calculations.

Our computational and experimental predictions are also coherent with other published experimental studies. It has been remarked that the effect of NPs on aggregation propensity is not only related to the increase of local concentration upon adsorption, but is also related to the peptide sequence itself.[99] More specifically, it was demonstrated that fullerenes can inhibit the fibril formation from Aβ by binding the region 16–21, KLVFF[56,57] with a mechanism that is also based of the affinity of PHE for the inorganic material[57] that has been found relevant also for other amyloidogenic peptides.[100] Moreover, it has been shown that hydrophobic nanoparticles slow down Aβ fibrillation under conditions when the hydrophobic core region LVFF is exposed.[101] What we find here is a very similar mechanism, although for an extended surface the balance between inhibition by fiber-conformation disruption and acceleration by increased surface concentration is likely more tilted toward the latter than for the fullerene molecules.

Recently, Crespi *et al.*[42] determined the crystal structure of the antibody Solanezumab (Eli Lilly) complexed to the mid-region (12–28) of the Aβ peptide. Clinical trials to evaluate Solanezumab as a possible drug to decrease the risk of Alzheimer's disease are under way. In that study it is shown that Solanezumab selectively binds the mid-region of the Aβ peptide, with the two PHE oriented parallel to each other, as we find here on the surface. Sequestration from the solution *via* high binding affinity and disruption of fiber-prone conformations are common features of this antibody and of gold surfaces, at least with regard to the truncated peptide considered here. The effect of the surface on the entire Aβ peptide cannot be extrapolated by these findings, and requires a specific investigation.

4. Conclusions

In this work, we have presented state-of-the-art enhanced sampling atomistic simulations of an amyloidogenic peptide interacting with a gold surface in water. In particular, we have characterized how the conformational ensemble of the peptide is modified by the interaction with the surface using a recently developed powerful analysis technique (sketch-map), and we have rationalized these changes in terms of the affinity of gold to phenylalanine. The main conclusion is that the surface depletes the conformational ensemble of fiber-like structures *via* a mechanism that is intermediate between induced fitting and conformational selection. Taking into account that the probability of assuming fiber-like conformations is correlated with fibrillation propensity,[44] we can conclude that the intrinsic effect of the surface is to *reduce* the fibrillation propensity of $A\beta_{16-22}$. However, this is contrasted by the capability of the surface to bind the peptide efficiently (as shown by binding free-energy results). This leads to a high peptide concentration at the surface, which may seed fibrillation.[39] Since the two pro-

cesses (depletion of fiber-like conformations and surface-induced nucleation) involve a different number of peptide molecules (the former acts on single peptides, the latter involves different peptides, depending on concentration),[102] we expect the resulting effect of the gold surface on $A\beta_{16-22}$ fibrillation propensity to be concentration dependent.[37] Despite this complexity, our results clearly highlight how the details of the peptide–surface interactions can determine the role of inorganic surfaces in affecting fibrillation, and may stimulate new strategies to exploit nanoparticles to control protein aggregation.

Acknowledgements

LB and SC acknowledge funding from MIUR for funding under the PRIN projects 20105ZZTSE and 2012A7LMS and the CINECA award under the ISCRA initiative, for the availability of high performance computing resources and support. AA and MP acknowledge funding from European Union under the Grant No. ERC-2009-AdG-247075 and from the National Centre of Competence in Research "Materials' Revolution: Computational Design and Discovery of Novel Materials" (NCCR-MARVEL) project.

References

1 D. M. Walsh and D. J. Selkoe, *J. Neurochem.*, 2007, **101**, 1172–1184.
2 E. Karran, M. Mercken and B. De Strooper, *Nat. Rev. Drug Discovery*, 2011, **10**, 698–712.
3 J. J. Balbach, Y. Ishii, O. N. Antzutkin, R. D. Leapman, N. W. Rizzo, F. Dyda, J. Reed and R. Tycko, *Biochemistry*, 2000, **39**, 13748–13759.
4 S. A. Petty and S. M. Decatur, *J. Am. Chem. Soc.*, 2005, **127**, 13488–13489.
5 K. Tao, J. Wang, P. Zhou, C. Wang, H. Xu, X. Zhao and J. R. Lu, *Langmuir*, 2011, **27**, 2723–2730.
6 K. Lu, J. Jacob, P. Thiyagarajan, V. P. Conticello and D. G. Lynn, *J. Am. Chem. Soc.*, 2003, **125**, 6391–6393.
7 H. Inouye, K. A. Gleason, D. Zhang, S. M. Decatur and D. A. Kirschner, *Proteins: Struct., Funct., Bioinf.*, 2010, **78**, 2306–2321.
8 D. J. Gordon, J. J. Balbach, R. Tycko and S. C. Meredith, *Biophys. J.*, 2004, **86**, 428–434.
9 A. Lakshmanan, D. W. Cheong, A. Accardo, E. Di Fabrizio, C. Riekel and C. A. Hauser, *Proc. Natl. Acad. Sci. U. S. A.*, 2013, **110**, 519–524.
10 U. F. Röhrig, A. Laio, N. Tantalo, M. Parrinello and R. Petronzio, *Biophys. J.*, 2006, **91**, 3217–3229.
11 F. Baftizadeh, F. Pietrucci, X. Biarnés and A. Laio, *Phys. Rev. Lett.*, 2013, **110**, 168103.
12 L. Xie, Y. Luo and G. Wei, *J. Phys. Chem. B*, 2013, **117**, 10149–10160.
13 W. M. Berhanu and U. H. Hansmann, *Protein Sci.*, 2012, **21**, 1837–1848.
14 P. H. Nguyen, M. S. Li, G. Stock, J. E. Straub and D. Thirumalai, *Proc. Natl. Acad. Sci. U. S. A.*, 2007, **104**, 111–116.
15 S. Gnanakaran, R. Nussinov and A. E. García, *J. Am. Chem. Soc.*, 2006, **128**, 2158–2159.
16 G. Favrin, A. Irbäck and S. Mohanty, *Biophys. J.*, 2004, **87**, 3657–3664.
17 S. Santini, G. Wei, N. Mousseau and P. Derreumaux, *Structure*, 2004, **12**, 1245–1255.
18 B. Ma and R. Nussinov, *Proc. Natl. Acad. Sci. U. S. A.*, 2002, **99**, 14126–14131.
19 P. H. Nguyen, M. S. Li and P. Derreumaux, *Phys. Chem. Chem. Phys.*, 2011, **13**, 9778–9788.
20 D. K. Klimov and D. Thirumalai, *Structure*, 2003, **11**, 295–307.
21 T. Takeda and D. K. Klimov, *J. Mol. Biol.*, 2007, **368**, 1202–1213.
22 L. O. Tjernberg, J. Näslund, F. Lindqvist, J. Johansson, A. R. Karlström, J. Thyberg, L. Terenius and C. Nordstedt, *J. Biol. Chem.*, 1996, **271**, 8545–8548.
23 A. Irbäck and S. Mitternacht, *Proteins: Struct., Funct., Bioinf.*, 2008, **71**, 207–214.
24 C. E. Giacomelli and W. Norde, *Macromol. Biosci.*, 2005, **5**, 401–407.
25 P. P. Mangione, G. Esposito, A. Relini, S. Raimondi, R. Porcari, S. Giorgetti, A. Corazza, F. Fogolari, A. Penco, Y. Goto, Y.-H. Lee, H. Yagi, C. Cecconi, M. M. Naqvi, J. D. Gillmore, P. N. Hawkins, F. Chiti, R. Rolandi, G. W. Taylor, M. B. Pepys, M. Stoppini and V. Bellotti, *J. Biol. Chem.*, 2013, **288**, 30917–30930.
26 M. Mahmoudi, H. R. Kalhor, S. Laurent and I. Lynch, *Nanoscale*, 2013, **5**, 2570–2588.
27 S. Rocha, A. F. Thünemann, M. D. C. Pereira, M. Coelho, H. Möhwald and G. Brezesinski, *Biophys. Chem.*, 2008, **137**, 35–42.
28 Q. Ma, G. Wei and X. Yang, *Nanoscale*, 2013, **5**, 10397–10403.
29 H. Lee, Y. Kim, A. Park and J.-M. Nam, *Small*, 2014, **10**, 1779–1789.
30 L. Xiao, D. Zhao, W.-H. Chan, M. M. F. Choi and H.-W. Li, *Biomaterials*, 2010, **31**, 91–98.
31 H. Li, Y. Luo, P. Derreumaux and G. Wei, *Biophys. J.*, 2011, **101**, 2267–2276.
32 H. Skaat, R. Chen, I. Grinberg and S. Margel, *Biomacromolecules*, 2012, **13**, 2662–2670.
33 Y.-H. Liao, Y.-J. Chang, Y. Yoshiike, Y.-C. Chang and Y.-R. Chen, *Small*, 2012, **8**, 3631–3639.
34 A. Antosova, Z. Gazova, D. Fedunova, E. Valusova, E. Bystrenova, F. Valle, Z. Daxnerova, F. Biscarini and M. Antalik, *Mater. Sci. Eng. C*, 2012, **32**, 2529–2535.
35 M. Zhang, X. Mao, Y. Yu, C.-X. Wang, Y.-L. Yang and C. Wang, *Adv. Mater.*, 2013, **25**, 3780–3801.
36 C. Cabaleiro-Lago, F. Quinlan-Pluck, I. Lynch, K. A. Dawson and S. Linse, *ACS Chem. Neurosci.*, 2010, **1**, 279–287.

37 R. Vácha, S. Linse and M. Lund, *J. Am. Chem. Soc.*, 2014, **136**, 11776–11782.
38 S. Linse, C. Cabaleiro-Lago, W.-F. Xue, I. Lynch, S. E. Radford and K. A. Dawson, *Proc. Natl. Acad. Sci. U. S. A.*, 2007, **104**, 8691–8696.
39 S. Auer, A. Trovato and M. Vendruscolo, *PLoS Comput. Biol.*, 2009, **5**, e1000458.
40 C. Cabaleiro-Lago, O. Szczepankiewicz and S. Linse, *Langmuir*, 2012, **28**, 1852–1857.
41 G. Brancolini, D. Toroz and S. Corni, *Nanoscale*, 2014, **6**, 7903–7911.
42 G. A. N. Crespi, S. J. Hermans, M. W. Parker and L. A. Miles, *Sci. Rep.*, 2015, **5**, 9649.
43 A. Morriss-Andrews, G. Bellesia and J.-E. Shea, *J. Chem. Phys.*, 2012, **137**, 145104.
44 G. Saracino, D. Cigognini, D. Silva, A. Caprini and F. Gelain, *Chem. Soc. Rev.*, 2013, **42**, 225–262.
45 L. Bellucci and S. Corni, *J. Phys. Chem. C*, 2014, **118**, 11357–11364.
46 J. L. Elechiguerra, J. Reyes-Gasga and M. J. Yacaman, *J. Mater. Chem.*, 2006, **16**, 3906.
47 U. H. Hansmann, *Chem. Phys. Lett.*, 1997, **281**, 140–150.
48 Y. Sugita and Y. Okamoto, *Chem. Phys. Lett.*, 1999, **314**, 141–151.
49 A. Laio and M. Parrinello, *Proc. Natl. Acad. Sci. U. S. A.*, 2002, **99**, 12562–12566.
50 J. F. Dama, M. Parrinello and G. A. Voth, *Phys. Rev. Lett.*, 2014, **112**, 240602.
51 M. Ceriotti, G. a. Tribello and M. Parrinello, *Proc. Natl. Acad. Sci. U. S. A.*, 2011, **108**, 13023–13028.
52 G. A. Tribello, M. Ceriotti and M. Parrinello, *Proc. Natl. Acad. Sci. U. S. A.*, 2012, **109**, 5196–5201.
53 P. Söderhjelm, G. A. Tribello and M. Parrinello, *Proc. Natl. Acad. Sci. U. S. A.*, 2012, **109**, 5170–5175.
54 M. Ceriotti, G. A. Tribello and M. Parrinello, *J. Chem. Theory Comput.*, 2013, **9**, 1521–1532.
55 A. Ardèvol, G. A. Tribello, M. Ceriotti and M. Parrinello, *J. Chem. Theory Comput.*, 2015, **11**, 1086–1093.
56 J. E. Kim and M. Lee, *Biochem. Biophys. Res. Commun.*, 2003, **303**, 576–579.
57 L. Xie, Y. Luo, D. Lin, W. Xi, X. Yang and G. Wei, *Nanoscale*, 2014, **6**, 9752–9762.
58 B. Hess, C. Kutzner, D. Van Der Spoel and E. Lindahl, *J. Chem. Theory Comput.*, 2008, **4**, 435–447.
59 M. Bonomi, D. Branduardi, G. Bussi, C. Camilloni, D. Provasi, P. Raiteri, D. Donadio, F. Marinelli, F. Pietrucci, R. Broglia and M. Parrinello, *Comput. Phys. Commun.*, 2009, **180**, 1961–1972.
60 W. Humphrey, A. Dalke and K. Schulten, *J. Mol. Graphics*, 1996, **14**, 33–38.
61 F. Iori, R. Di Felice, E. Molinari and S. Corni, *J. Comput. Chem.*, 2009, **30**, 1465–1476.
62 F. Iori and S. Corni, *J. Comput. Chem.*, 2008, **29**, 1656–1666.
63 D. J. Rosenman, C. R. Connors, W. Chen, C. Wang and A. E. García, *J. Mol. Biol.*, 2013, **425**, 3338–3359.
64 S. R. Gerben, J. A. Lemkul, A. M. Brown and D. R. Bevan, *J. Biomol. Struct. Dyn.*, 2014, **32**, 1817–1832.
65 H. Berendsen, J. Postma, W. Van Gunsteren and J. Hermans, *Intermol. Forces*, 1981, **11**, 331–342.
66 B. Hess, *J. Chem. Theory Comput.*, 2008, **4**, 116–122.
67 G. Bussi, D. Donadio and M. Parrinello, *J. Chem. Phys.*, 2007, **126**, 014101.
68 G. Bussi, A. Laio and M. Parrinello, *Phys. Rev. Lett.*, 2006, **96**, 090601.
69 M. Bonomi, D. Branduardi, G. Bussi, C. Camilloni, D. Provasi, P. Raiteri, D. Donadio, F. Marinelli, F. Pietrucci, R. A. Broglia and M. Parrinello, *Comput. Phys. Commun.*, 2009, **180**, 1961–1972.
70 P. Tiwary and M. Parrinello, *J. Phys. Chem. B*, 2015, **119**, 736–742.
71 J. Schneider and L. Colombi Ciacchi, *J. Am. Chem. Soc.*, 2012, **134**, 2407–2413.
72 S. Mauri, R. Pandey, I. Rzeźnicka, H. Lu, M. Bonn and T. Weidner, *Front. Phys.*, 2015, **3**, 51.
73 S. J. Roeters, C. N. van Dijk, A. Torres-Knoop, E. H. Backus, R. K. Campen, M. Bonn and S. Woutersen, *J. Phys. Chem. A*, 2013, **117**, 6311–6322.
74 M. Hnilova, E. E. Oren, U. O. S. Seker, B. R. Wilson, S. Collino, J. S. Evans, C. Tamerler and M. Sarikaya, *Langmuir*, 2008, **24**, 12440–12445.
75 Z. Tang, J. P. Palafox-Hernandez, W.-C. Law, Z. E. Hughes, M. T. Swihart, P. N. Prasad, M. R. Knecht and T. R. Walsh, *ACS Nano*, 2013, **7**, 9632–9646.
76 L. B. Wright, P. M. Rodger, S. Corni and T. R. Walsh, *J. Chem. Theory Comput.*, 2013, **9**, 1616–1630.
77 L. B. Wright, P. M. Rodger, T. R. Walsh and S. Corni, *J. Phys. Chem. C*, 2013, **117**, 24292–24306.
78 L. B. Wright, J. P. Palafox-Hernandez, P. M. Rodger, S. Corni and T. R. Walsh, *Chem. Sci.*, 2015, **6**, 5204–5214.
79 J. P. Palafox-Hernandez, Z. Tang, Z. E. Hughes, Y. Li, M. T. Swihart, P. N. Prasad, T. R. Walsh and M. R. Knecht, *Chem. Mater.*, 2014, **26**, 4960–4969.
80 G. Bellesia and J.-E. Shea, *Biophys. J.*, 2009, **96**, 875–886.
81 P. E. Wright and H. J. Dyson, *Curr. Opin. Struct. Biol.*, 2009, **19**, 31–38.
82 N. London, D. Movshovitz-Attias and O. Schueler-Furman, *Structure*, 2010, **18**, 188–199.
83 D. D. Boehr and P. E. Wright, *Science*, 2008, **320**, 1429–1430.
84 S. Kumar, B. Ma, C. J. Tsai, N. Sinha and R. Nussinov, *Protein Sci.*, 2000, **9**, 10–19.
85 D. E. Koshland, *Proc. Natl. Acad. Sci. U. S. A.*, 1958, **44**, 98–104.
86 J. Colletier, A. Laganowsky, M. Landau, M. Zhao, A. B. Soriaga, L. Goldschmidt, D. Flot, D. Cascio, M. Sawaya and D. Eisenberg, *Proc. Natl. Acad. Sci. U. S. A.*, 2011, **108**, 16938–16943.
87 M. Landau, M. R. Sawaya, K. F. Faull, A. Laganowsky, L. Jiang, S. A. Sievers, J. Liu, J. R. Barrio and D. Eisenberg, *PLoS Biol.*, 2011, **9**, e1001080.
88 M. Hoefling, F. Iori, S. Corni and K.-E. Gottschalk, *Langmuir*, 2010, **26**, 8347–8351.

89 J. E. Baio, T. Weidner, G. Interlandi, C. Mendoza-Barrera, H. E. Canavan, R. Michel and D. G. Castner, *J. Vac. Sci. Technol., B*, 2011, **29**, 04D113.
90 T. Weidner, A. Kramer, C. Bruhn, M. Zharnikov, A. Shaporenko, U. Siemeling and F. Trager, *Dalton Trans.*, 2006, 2767–2777.
91 Y. R. Shen, *The Principles of Nonlinear Optics*, Wiley, New York, 1st edn, 1984.
92 L. Fu, Z. G. Wang and E. C. Y. Yan, *Chirality*, 2014, **26**, 521–524.
93 B. Ding, A. Panahi, J. J. Ho, J. E. Laaser, C. L. Brooks, M. T. Zanni and Z. Chen, *J. Am. Chem. Soc.*, 2015, **137**, 10190–10198.
94 D. Schach, C. Globisch, S. J. Roeters, S. Woutersen, A. Fuchs, C. K. Weiss, E. H. G. Backus, K. Landfester, M. Bonn, C. Peter and T. Weidner, *J. Chem. Phys.*, 2014, **141**, 22D517.
95 R. Hennig, J. Heidrich, M. Saur, L. Schmuser, S. J. Roeters, N. Hellmann, S. Woutersen, M. Bonn, T. Weidner, J. Markl and D. Schneider, *Nat. Commun.*, 2015, **6**, 7018.
96 A. P. Boughton, P. Yang, V. M. Tesmer, B. Ding, J. J. G. Tesmer and Z. Chen, *Proc. Natl. Acad. Sci. U. S. A.*, 2011, **108**, E667–E673.
97 K. Nguyen, J. King and Z. Chen, *J. Phys. Chem. B*, 2010, **114**, 8291–8300.
98 L. Baugh, T. Weidner, J. E. Baio, P.-C. T. Nguyen, L. J. Gamble, P. S. Stayton and D. G. Castner, *Langmuir*, 2010, **26**, 16434–16441.
99 S. C. Wagner, M. Roskamp, M. Pallerla, R. R. Araghi, S. Schlecht and B. Koksch, *Small*, 2010, **6**, 1321–1328.
100 N. Todorova, A. J. Makarucha, N. D. M. Hine, A. A. Mostofi and I. Yarovsky, *PLoS Comput. Biol.*, 2013, **9**, e1003360.
101 M. Ghavami, M. Rezaei, R. Ejtehadi, M. Lotfi, M. A. Shokrgozar, B. Abd Emamy, J. Raush and M. Mahmoudi, *ACS Chem. Neurosci.*, 2013, **4**, 375–378.
102 D. Kashchiev, R. Cabriolu and S. Auer, *J. Am. Chem. Soc.*, 2013, **135**, 1531–1539.